Environmental Fluid Mechanics (2023) 23:1–18
https://doi.org/10.1007/s10652-022-09903-z

ORIGINAL ARTICLE

Interactions between emergent and submerged porous horseshoe elements and open channel flows

Hubert Chanson[1] · William Johnson[2]

Received: 6 May 2022 / Accepted: 3 November 2022 / Published online: 17 November 2022

Abstract
The Australian Aboriginals built fish traps and weirs over a long period of time, and there is a wide variety of structures. Herein this study focuses on rock fish traps constructed in inland waterways. A common shape was a horseshoe design convex in shape and opened downstream. In this study, some basic physical modelling of rock fish trap models was conducted under controlled flow conditions. A generic horseshoe element shape was selected, with a range of porosity, consistent with the rock fish trap construction. Flow conditions were tested from low partial submergence to complete submergence, corresponding to large flood events. The results give some seminal insights into the hydrodynamics of these fish traps and provide some physically-based understanding of their operation and purpose.

Article Highlights

- Semi-circular horseshoe elements open downstream were tested physically.
- A broad range of free-surface flow patterns were observed with porous and impervious elements.
- The element porosity modified the recirculation region and flow patterns.
- Interactions between adjacent horseshoe structures were tested experimentally.

Keywords Horseshoe roughness · Open channel flows · Physical modelling · Porous rock fish trap · Three-dimensional flows · Wake flows

✉ Hubert Chanson
h.chanson@uq.edu.au

1 Hydraulic Engineering, School of Civil Engineering, The University of Queensland, Brisbane, QLD 4072, Australia

2 School of Civil Engineering, The University of Queensland, Brisbane, QLD 4072, Australia

1 Introduction

The Australian indigenous people built weirs and fish traps for a long period time, with a wide range of designs [2, 14]. Along inland river systems, a number of rock fish traps were built with a broad range of shapes [12]. Some structures included long funnelled channels [8], while other traps were irregular in shape [1, 12]. A number of rock fish traps were opened to the downstream and in convex in shape facing upstream [7, 12] (Fig. 1). Such rock fish traps were permanent structures, interacting with the river flow for a broad range of water depths and velocities, from fully-submerged to completely dry.

Along the inland streams, the rock fish traps were primarily used by the indigenous Australians when the water levels was less than waist height [7]. For larger flows, the stability of the people in the river waters would be an issue, preventing any individual to stand, move and fish in the riverine environment [18], [6]. In turn, the flow conditions during which fishing was possible in the rock fish traps would have been limited, in terms of both fish attraction conditions and safety of the individuals. The fish traps might have acted as secondary roles. For example, during dry periods, the traps could have acted as rock holes to retain waters, recharging the aquifer, acting as drinking holes for the fauna and potentially becoming hunting grounds for indigenous Australians. Further, during very large floods, the rock fish traps became large bed roughness elements, likely generating strong secondary currents and inducing turbulent dissipation. It is highly probable that the resulting water column mixing also enhanced the overall water quality and increased the sediment transport capacity of the stream.

Herein, the physical modelling of generic rock fish traps was performed under controlled flow conditions, based upon a Froude similitude. The aim of the study was to gain a sound physical understanding of the hydraulic operation of rock fish traps, across a broad range of submergence ratio, ranging from low flows and emergent fish traps to major floods with fully-submerged structures.

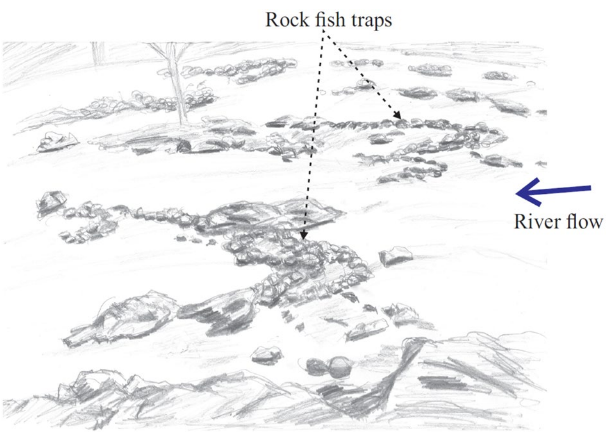

Fig. 1 Sketch of Australian indigenous rock fish traps on the Darling River (after an original glass plate negative)

2 Physical modelling: instrumentation and methodology

2.1 Experimental facility and boundary conditions

The physical experiments were performed in two identical 3.2 m long, 0.4 m wide horizontal channels (Fig. 2A). The channels consisted of a smooth PVC bed and smooth glass sidewalls. Water was supplied by a constant head tank, feeding an intake structure with a three-dimensional convergent leading into the horizontal channel. In one channel, the discharge was measured using a volume per time technique (Channel 1) well adapted to small flow rates [16]. In the other channel, the discharge was measured using an orifice meter installed in the supply line (Channel 2), built based upon British Standards [4]. In both channels, the water depths were measured using pointer gauges. More, photographic and cinematographic records were undertaken with a dSLR Pentax™ K-3 camera, a Casio™ EX-10 Exilim digital camera and a Sony™ RX100VA digital camera. The latters could record high-speed video movies anywhere between 25 and 480 fps.

Several boundary conditions were tested. The reference configuration was a smooth channel without element. Several horseshoe elements models were manufactured as generic rock fish trap structures (Fig. 2B, Table 1). All had a cylindrical D-shape opened to the downstream end. The diameter was D = 0.10 m, the height was H = 0.050 m and the thickness was t = 0.020 m. The horseshoe element models were selected as 1:20 scale model of typical Australian aboriginal fish traps, and the geometric scaling ratio was chosen to minimise the blockage ratio with one model only in the flume. One model (M1) was impervious, while the others were porous. The values of porosity were selected from a plain impervious model (M1) with zero porosity to a 27% porosity design with random patterns which would be typical of Australian aboriginal fish trap constructions. Most porous element testing was conducted with the models M3 and M4, the former being representative of a man-made structure (e.g. built in gabions) and the latter being more typical of natural rock arrangements, as illustrated in Fig. 1. The models were 3D printed, with an accuracy of 0.1 mm, and fixed to the invert with magnets.

2.2 Methods and experimental conditions

The horseshoe elements were installed 1.2 m downstream of the upstream end of the channel. The upstream water depth was measured 0.26 m upstream of the horseshoe element, while downstream depth was recorded 1.35 m downstream of the element on the channel centreline.

Four configurations were used: one element installed on the channel centreline (Fig. 2A), two elements, three elements, and four elements installed side by side, in a full length linear weir arrangement (Fig. 3). Figure 3 shows a photographic comparison between four elements installed side by side and a non-linear weir at a dam spillway crest. Figure 3 highlights a striking similarity despite the absence of engineering interactions between the two worlds.

The measurements were recorded for steady discharges within $0.0005\ \mathrm{m^3/s} < Q < 0.050\ \mathrm{m^3/s}$, corresponding to inflow depths within about $0.1 < d_1/H < 3.2$, with H the vertical horseshoe element height. Visual observations were assisted with dye injection (Tintex™ food dye), using a dSLR Pentax™ K-3, a digital camera Casio™

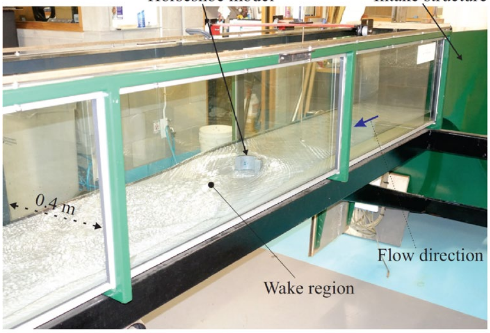

(A) Photograph of the experimental flume (Channel 1) with a single horseshoe element- Flow conditions: Q = 0.0058 m^3/s, d_1 = 0.0465 m, D/B = 0.25, Impervious model (M1)

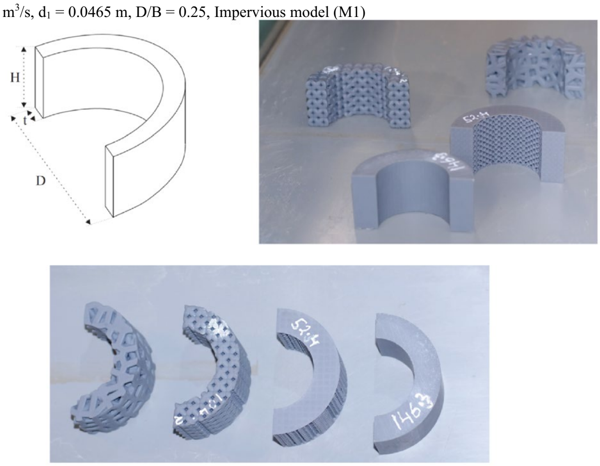

(B) Sketch and photographs of horseshoe elements - In bottom photograph, models M4, M3, M2 and M1 from left to right (Table 1)

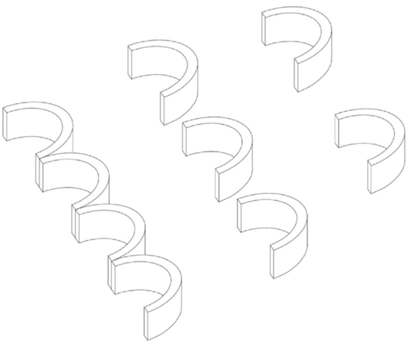

(C) Schematic of the layout of the roughness elements with 4 elements, 3 elements and 2 elements from left to right

Fig. 2 Experimental channel and horseshoe element design

Table 1 Horseshoe element models

Model	Height H (m)	Diameter D (m)	Annular thickness t (m)	Mass m (kg) (*)	Porosity	Shape
M1	0.051	0.100	0.020	0.1463	0	Plain
M2				0.0524	0.64	4 mm hole lattice
M3				0.1042	0.29	8 mm hole lattice flow through
M4				0.1062	0.27	Random pattern/flow through

*Without metallic plate

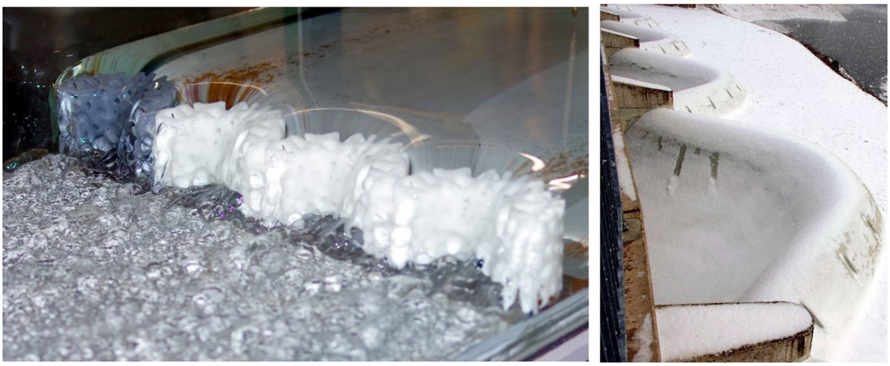

Fig. 3 Non-linear weir arrangement made by Four porous horseshoe elements installed side by side—Flow conditions: $Q = 0.003$ m^3/s, $d_1 = 0.0695$ m, $(\Sigma D)/B = 0$, Four porous models (M4)—Inset (Right): non-linear weir crest at Urft Dam, Germany on 22 February 2013 under the snow

Exilim EX10, a digital camera Sony™ RX100 VA and Apple™ iPhone. A series of video movies are in the Digital Appendix (Appendix 1, Table 3).

3 Hydraulics of single horseshoe element

3.1 Flow patterns

The visual observations showed some basic differences in terms of flow patterns between the impervious horseshoe model (M1) and the porous models. Table 2 summarises the key flow features.

With the impervious (plain) model M1, a total of six basic flow patterns were seen as a function of the dimensionless ratio d_c/H, with d_c the critical flow depth: $d_c = (q^2/g)^{1/3}$, q the unit discharge and g the gravity acceleration (Fig. 4). For small discharges ($d_c/H < 0.18$, Regime L), the flow upstream of, around and downstream of the horseshoe element was subcritical. A couple of key flow features were the strong recirculation motion in the open semi-circular cavity immediately behind the element, as well as a marked von Karman street of vortices in the wake. Both features are illustrated in Fig. 3A and Movie CIMG7515.mov (Appendix 1, Table 3). The flow separation alternated between the right and left outer edge, inducing an oscillating wake. The vortices were shed alternately, resulting in a pattern of large-scale vortical structures rotating in opposite directions in the downstream wake (Fig. 3A). The observations of vortex shedding indicated a dimensionless frequency about: $F \times D/V_1 \approx 0.45$, with V_1 the upstream flow velocity. The data may be compared to the vortex shedding frequency of a circular cylinder of 0.2 [5, 11]. Such an oscillating wake flow pattern was observed to be conducive of fish attraction and upstream fish attraction [3, 10] and well adapted to the fish trap operation.

For larger flows ($0.18 < d_c/H < 0.4$–0.5, Regime NC1), the upstream flow motion presented a characteristic horseshoe surface pattern around the element (Fig. 3B). Moderately-weak shock waves originated from the downstream ends of the semi-circular obstacle, implying that the flow transitioned from subcritical (upstream) to critical and supercritical as it flowed around the horseshoe element. Behind the rock fish trap model, the recirculation remained strong in the cavity region. With increasing discharge and

Table 2 Experimental flow patterns with single horseshoe element models

Flow regime	Model	d_c/H	Flow features
L	M1	<0.18	No choking. Subcritical flow with von Karman street of vortices in the wake
NC1		0.18–0.4–0.5	Slight chock. Horseshoe free-surface pattern. Mild shock waves downstream
A		0.5–0.6	Chocking. Strong horseshoe free-surface pattern. Strong shock waves downstream
NC2		0.6–0.9	Submerged element. Strong interference between overflow over the element and cavity recirculation
E		0.9–2	Strong horseshoe free-surface pattern. Detached shock waves downstream
F		>2	Fully-submerged element acting as isolated roughness
L	M2-M4	<0.3	No choking. Subcritical flow with von Karman street of vortices in the wake
C		0.3–1.2	Horseshoe free-surface pattern. Interactions between seepage and recirculation region,. Weak shock waves downstream
D		1.2–1.3	Submerged element. Interactions between seepage, overflow and recirculation region
E		1.3–3	Strong horseshoe free-surface pattern. Detached shock waves downstream
F		>3	Fully-submerged element acting as isolated roughness

Fig. 4 Flow patterns with an impervious horseshoe element (Flow direction from right to left)—(**A**) ▶ Regime L ($d_c/H < 0.18$) with von Karman street of vortices; (**B**) Regime NC1 ($0.18 < d_c/H < 0.4$–0.5) with weak shock waves originating from ends; (**C**) Regime A ($0.5 < d_c/H < 0.6$) with strong shock waves intersecting (non-submerged element); (**D**) Regime NC2 ($0.6 < d_c/H < 0.9$) interference between overflow and recirculation region; (**E**) Regime E ($0.9 < d_c/H < 2$) with detached shock waves; (**F**) Regime F ($d_c/H > 2$–2.2) with fully-submerged element acting as large roughness

with the element remaining un-submerged ($0.5 < d_c/H < 0.6$, Regime A), a marked free-surface pattern with a strong horseshoe shape was observed upstream of and around the model. Strong cross-waves originated from the cavity flow with a characteristic V-shape (Fig. 3C). A similar free-surface pattern was observed by [20] around an un-submerged rectangular building.

For larger discharges, the fish trap model became submerged. In Regime NC2 ($0.6 < d_c/H < 0.9$), some interference developed between the overflow over the element and the cavity recirculation. These features are illustrated in Fig. 3D and Movie IMGP7352.mov (Appendix 1, Table 3). The interactions between cavity recirculation and overflow were presented features similar to earlier observations at horseshoe waterfalls [9, 13] and horseshoe weir [15]. With even large discharges, the free-surface pattern presented a strong horseshoe free-surface pattern and detached shock waves ($0.9 < d_c/H < 2$, Regime E) (Fig. 3E). At large discharges, the element became fully-submerged: i.e., Regime F ($d_c/H > 2$–2.2). The horseshoe element then acted as a large isolated roughness, and the free-surface elevation dropped from upstream to downstream, as some turbulent energy dissipation occurred. (Fig. 3F).

For the porous horseshoe elements, a key feature was the seepage flow through the structure, which interacted with the recirculation region, typically by reducing the strength of the recirculation. In fluid dynamics, fluid injection in the separated region reduces substantially the drag for both two- and three-dimensional bodies (Wood 1964, Verron and Michel 1984, Naudascher and Rockwell 1994). A similar change in form drag was expected herein.

In the present study, the same flow patterns were observed for all three porous horseshoe models. Figure 5 presents photographs of the flow patterns for Model M4, and illustrations for Model M3 are shown in Appendix 2. For low discharges and shallow-water flows, some large-scale vortex shedding was seen, with a von Karman street of vortices (Fig. 5A, Regime L). With larger flow rates, a horseshoe free-surface pattern was seen upstream and around the obstacle. In Regime C, some weak shock waves were observed with some interaction between seepage and recirculation flows. This is seen in Fig. 5B and Movie IMGP7919.mov (Appendix 1, Table 3). When the horseshoe model started to be overtopped, the overtopping typically seeped into the porous material, and the transition from partially-submerged to fully-submerged was less marked than with the impervious model. For higher inflows (Regime D), the interactions between seepage, overflow and recirculation motion yielded a complicated downstream flow with a very turbulent broad wake region (Fig. 5C). With a further increase in discharge, the shock waves became stronger and detached from the element (Fig. 5D, Regime E). The Movie IMGP8025.mov presents the flow pattern, with dye injection highlighting the recirculation region (Appendix 1, Table 3). Finally, for large flows, the horseshoe element became fully-submerged (Fig. 5E, Regime F).

Wűthrich et al. [17] observed related flow patterns around some un-submerged porous rectangular building models. Taddei et al. (2016) and Gillies et al. (2021) reported some major changes in the downstream velocity field and turbulence, between impervious and

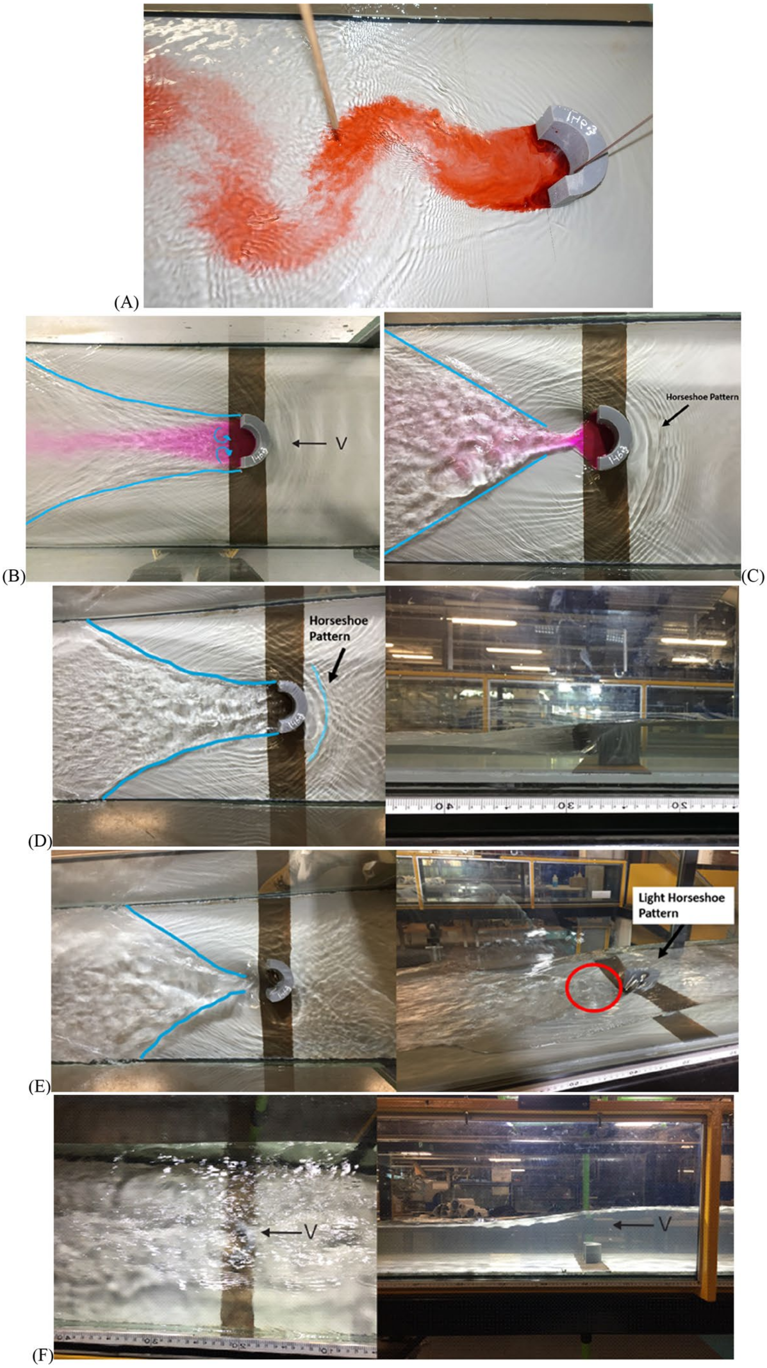
(A)
(B)
V
(C)
Horseshoe Pattern
(D)
Horseshoe Pattern
(E)
Light Horseshoe Pattern
(F)
V
V

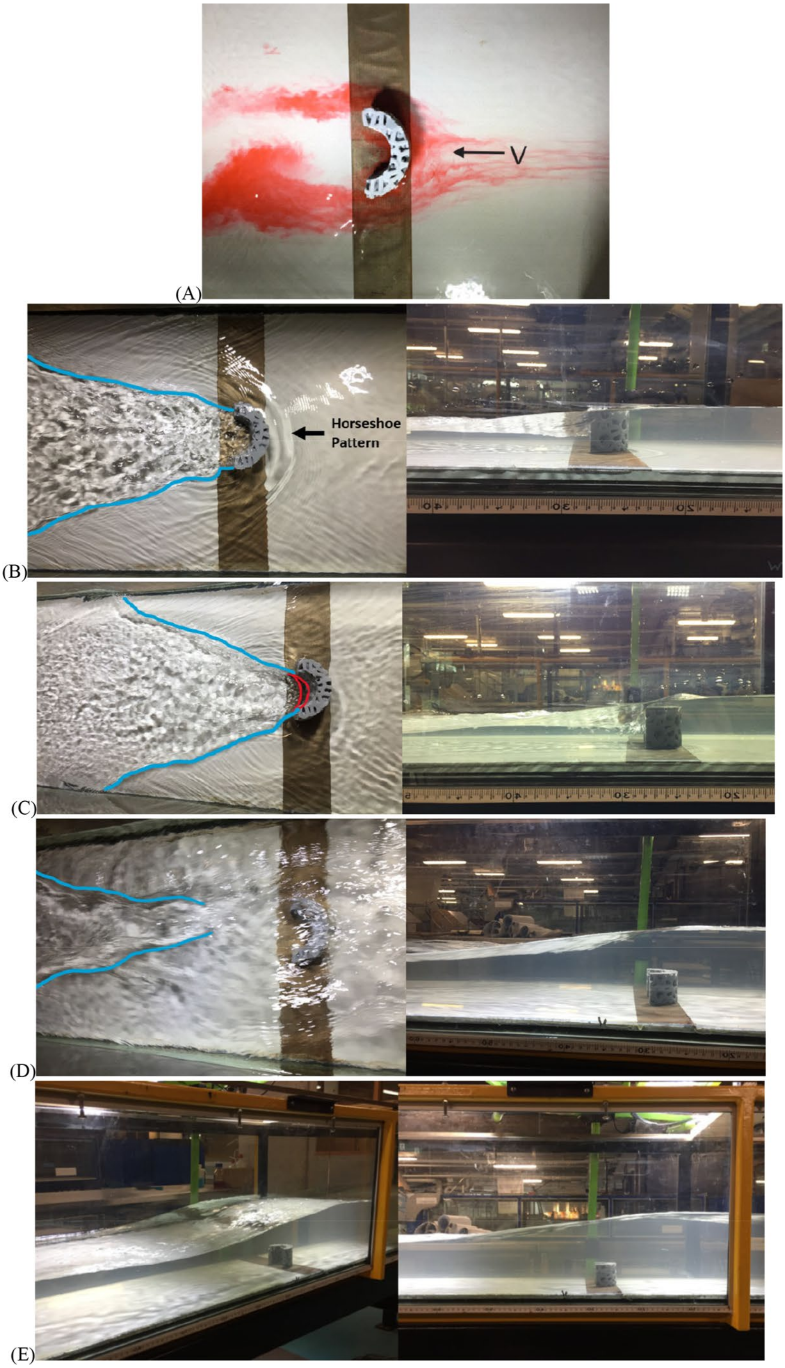

Fig. 5 Basic flow patterns with a pervious horseshoe element (M4), with flow direction from right to left (unless indicated). (**A**) Regime L ($d_1/H < 0.3$) with von Karman street of vortices; (**B**) Regime C ($0.3 < d_1/H < 1.2$) with weak shock waves and interaction between seepage and recirculation region; (**C**) Regime D ($1.2 < d_1/H < 1.3$); with interactions between seepage, overflow and recirculation region (**D**) Regime E ($1.3 < d_1/H < 3$) with detached shock waves; (**E**) Regime F ($d_1/H > 3$) with fully-submerged element acting as large roughness

permeable cylinders and cubes, associated with substantial reduction in drag and invert erosion with porous structures.

3.2 Relationship between afflux and discharge

The afflux is the rise in upstream water level above normal level, i.e. natural flood level in absence of structure. In the United States, it is commonly referred to as maximum backwater. The afflux provides a quantitative measure of the upstream flooding caused by a hydraulic structure (e.g. culvert, weir) [5], Chanson and Leng 2021). It is linked to the rate of energy dissipation. In the current study, the presence of the horseshoe element induced a substantial increase in upstream water compared to the smooth flume, for an identical unit discharge, hence some afflux (Fig. 6). Figure 6 illustrates the dimensionless relationship between upstream water levels and unit discharge for four channel boundary configurations.

Assuming a two-dimensional flow upstream and downstream of the fish trap model, the momentum principle may be applied in an integral form:

$$\rho \times Q \times (V_2 - V_1) = \frac{1}{2} \times \rho \times g \times (d_1^2 - d_2^2) \times B - F_{drag} \tag{1}$$

With ρ the flow density, Q the water discharge, B the channel width, V the flow velocity, F_{drag} the total drag force exerted by the element on the flow, and the subscripts 1 and 2 referring to the upstream and downstream flow conditions respectively. After transformation, the dimensionless form drag coefficient C_D of the horseshoe element may thus be expressed

$$C_D = \frac{F_{drag}}{\frac{1}{2} \times \rho \times V_1^2 \times A_H} \tag{2}$$

with V_1 the upstream velocity and A_H the projected area of the horseshoe element, i.e. $A_H = H \times D$ for a submerged element and $A_H = d_1 \times D$ otherwise. While Eq. (2) was

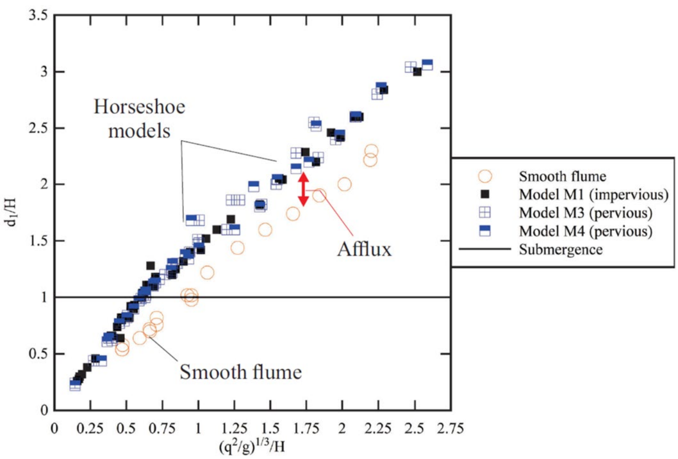

Fig. 6 Dimensionless relationship between upstream water depth d_1 and unit discharge q for the smooth flume, impervious horseshoe model M1 and impervious horseshoe models M3 and M4

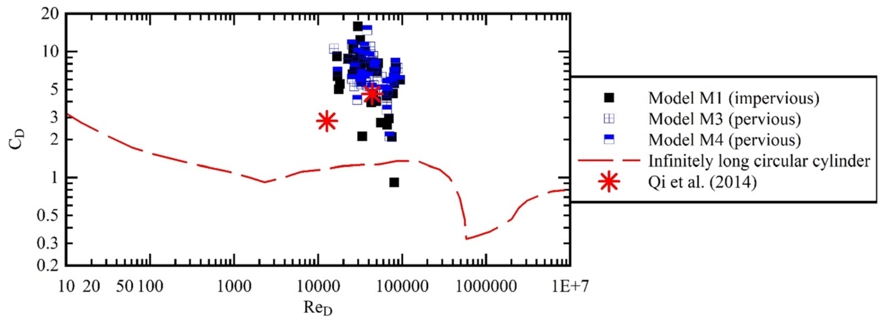

Fig. 7 Drag coefficient C_D as a function of the Reynolds number $Re_D = \rho \times V_1 \times D/\mu$ for impervious horseshoe model M1 and impervious horseshoe models M3 and M4—Comparison with data for square cylinders in open channels and infinitely long cylinders

developed for two-dimensional flows, present results are presented in Fig. 7 for the full range of submergence ratio. Figure 7 includes also some load cell data with a square cylinder in an open channel with a comparable blockage ratio (QI et al. 2014) and the drag coefficient data of infinitely long cylinder. Overall, the present data sets showed large drag coefficients, linked to the choking and critical flow conditions around the horseshoe element as well as the turbulent dissipation in the shockwaves and cross-waves downstream.

4 Discussion: interactions between side-by-side horseshoe elements

4.1 Interactions between separated horseshoe elements

Additional experiments were conducted with two, three and four horseshoe elements installed side-by-side. While the last one is discussed in the next sub-section, the flow patterns and performances of two and three elements are developed herein.

The visual observations showed some major interactions between the side-by-side elements (Fig. 8). The free-surface patterns presented two main differences with those observed with a single element. First, the narrow gap between the elements was conducive of choking conditions for a much wider range of discharges. In turn, this induced a greater afflux and higher upstream water level than for a single element and same discharge. Second, the downstream flow presented some more complicated pattern of oblique hydraulic jumps and shock waves criss-crossing the channel.

Typical photographs of the interactions between side-by-side porous elements are presented in Figs. 8A and 8B. Figure 8C shows the dimensionless relationship between the upstream water depth and discharge, with d_c the critical flow depth calculated using the upstream channel width $B = 0.4$ m.

4.2 Hydraulics of four side-by-side horseshoe elements

A series of experiments were conducted with four side-by-side horseshoe elements. The configuration corresponded to a porous linear weir, with a total weir crest development $2 \times \pi \times D$. It is shown in Fig. 5A and Movie IMGP0738.mov (Appendix 1).

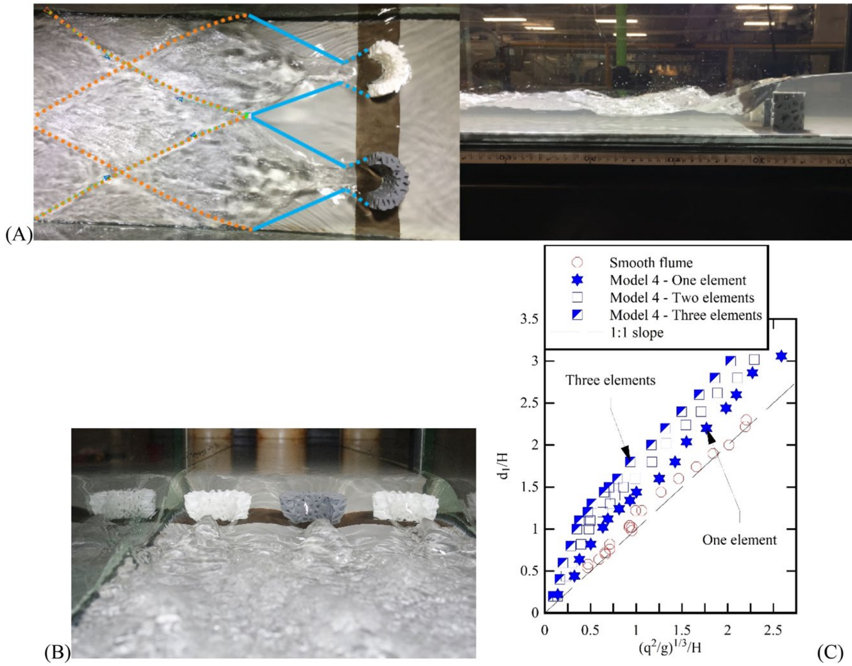

Fig. 8 Interactions between side-by-side porous horseshoe elements—(**A**) Free-surface pattern with two porous models (Model M4) for $Q = 0.0112 m^3/s$; (**B**) Looking upstream of flow past three porous models (Model M4) for $Q = 0.0099$ m^3/s; (**C**) Dimensionless relationship between upstream water depth d_1/H and unit discharge $(q^2/g)^{1/3}/H$ for porous horseshoe models

The flow pattern was consistent with that on a continuous non-linear weir (Fig. 5B). This is also nicely illustrated in Movie IMGP0738.mov (Appendix 1, Table 3). Little difference was observed between the impervious and porous weirs, except at very low flow rates ($Q < 0.0004$ m^3/s) when water seeped through the porous "weir. Dimensionless results are presented in Fig. 9A, in terms of the relationship between the upstream water depth and unit discharge, and the data are compared with an arrangement of four impervious side-by-side horseshoe elements, a single horseshoe element and no element (smooth flume). Overall, the data illustrated the impact of the whole blockage of the channel width by the four horseshoe elements installed side-by-side.

The dimensionless relationship between the upstream water level and discharge is shown in Fig. 8B, in which the critical flow depth d_c' was calculated in terms of the non-linear weir development:

$$d'_c = \sqrt[3]{\frac{Q^2}{g \times (2 \times \pi \times D)^2}} \text{ four horseshoe elements side-by-side} \tag{3}$$

In Fig. 9B, the present data are compared with the relationships for broad-crested weir and two-dimensional sharp-crested weir (BOES 1976, Chanson 2004). Within the range of investigated flow conditions, the current data compared more favourably with the broad-crested weir relationship.

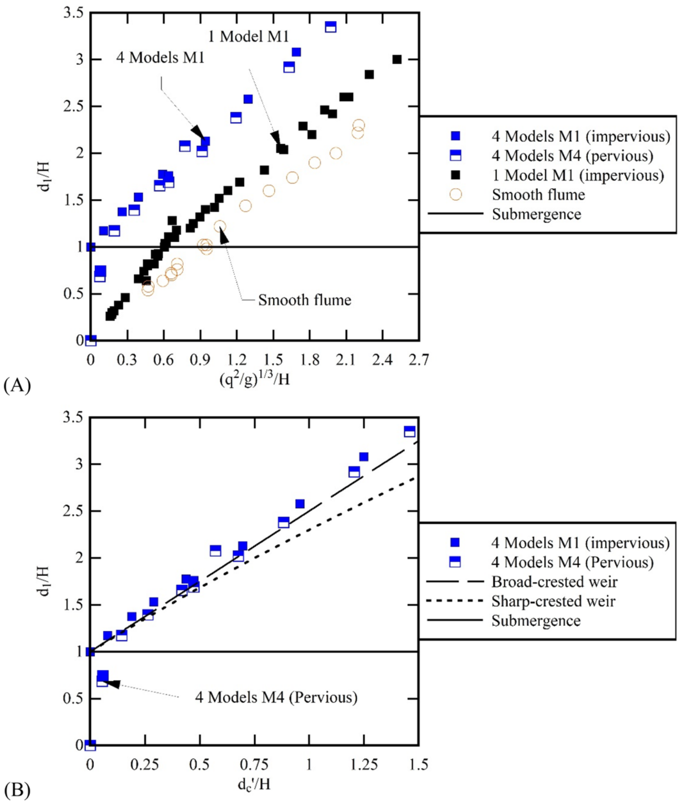

Fig. 9 Discharge characteristics of four side-by-side horseshoe elements (Models M1 and M4)—(**A**) Dimensionless upstream water depth d_1/H as a function of the dimensionless unit discharge including a comparison with smooth flume (no model) and single horseshoe element (Model M1) data; (**B**) Dimensionless upstream water depth d_1/H as a function of the dimensionless water discharge d_c'/H calculated in terms of the non-linear weir length

5 Conclusion

The present study was motivated by fascinating hydraulic structures, in the form of rock fish traps built by indigenous Australians along inland waterways. A common shape was a horseshoe design opened downstream. Herein, some physical modelling of rock fish trap models was conducted under controlled flow conditions. A generic semi-circular horseshoe shape was selected, with a range of porosity consistent with the rock fish trap construction.

The physical observations showed a broad range of flow patterns, depending upon the submergence ratio d_1/H, and to a lesser extent the porosity. In shallow waters, some large-scale vortical structures were observed, as a result of alternate vortex shedding downstream of the horseshoe element. The von Karman street of vortices was conducive to upstream fish attraction into the fish trap enclosure. For larger flows, seminal differences were seen between the impervious and pervious horseshoe model. The porosity of the element facilitated some interactions between the seepage and recirculation region, leading to changes in the wake region and its turbulence. The relationship between upstream water level and water flow rate indicated a substantial increase in upstream water depth (i.e. some afflux) compared to a smooth channel configuration. The application of the equation of conservation of momentum yielded quantitative estimate of the drag coefficient of the structures.

Further investigations considered the interactions between adjacent horseshoe structures. The data showed restricted flow passage around the horseshoe structures, with choking flow conditions and the turbulent dissipation in shockwaves and cross-waves downstream.

The present work should be considered as a preliminary work to be complemented by field measurements in real-life prototype structures. Further studies should further test the impact of different tailwater conditions, the interactions with fauna and flora, and sediment processes.

Appendix 1: Digital Appendix

Visual observations were recorded using a dSLR Pentax™ K-3 and a digital camera Casio™ Exilim EX10. Table 3 describes each video movie available in the digital appendix.

Table 3 Video observations of flow patterns around horseshoe elements

Filename	Camera	Physical model	Description
CIMG7515.jpg	Casio EX10	M1	Dye injection highlighting the cavity recirculation and von Karman Street of vortices ($d_c/H = 0.078$, regime L)
IMGP7352.mov	Pentax K-3	M1	Horseshoe free-surface pattern around the impervious semi-circular element ($d_c/H \sim 0.8$, regime NC)
IMGP7736.mov	Pentax K-3	M3	Dye injection in cavity for relatively large flow rate ($d_c/H = 1.44$, regime E)
IMGP7919.mov	Pentax K-3	M4	Dye injection in cavity for moderate flow rate ($d_c/H = 0.62$, regime C)
IMGP8025.mov	Pentax K-3	M4	Dye injection in cavity for large flow rate ($d_c/H = 1.77$, regime E)
IMGP0738.mov	Pentax K-3	4 × M4	Overflow above 4 elements side-by-side ($d_c/H = 0.76$)

Appendix 2: Flow patterns for porous model M3

Figure 10 presents photographs of the main flow patterns of the free-surface flow as the porous model M3, with 8 mm hole lattice flow through.

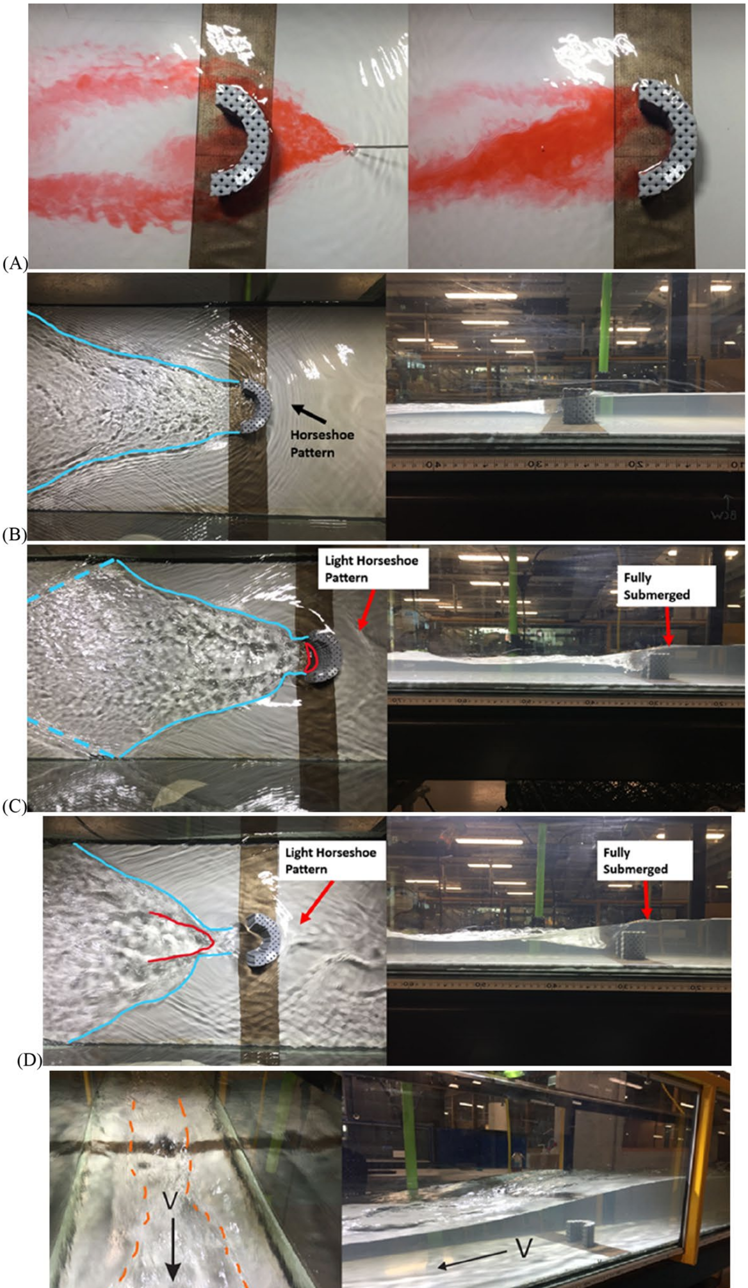

Fig. 10 Basic flow patterns with a pervious horseshoe element (M3), with flow direction from right to left (unless indicated). (**A**) Regime L ($d_1/H<0.3$) with von Karman street of vortices; (**B**) Regime C ($0.3<d_1/H<1.2$) with weak shock waves and interaction between seepage and recirculation region; (**C**) Regime D ($1.2<d_1/H<1.3$); with interactions between seepage, overflow and recirculation region (**D**) Regime E ($1.3<d_1/H<3$) with detached shock waves; (**E**) Regime F ($d_1/H>3$) with fully-submerged element acting as large roughness

Supplementary Information The online version contains supplementary material available at https://doi.org/10.1007/s10652-022-09903-z.

Acknowledgements The authors acknowledge the technical assistance of Jason VAN DER GEVEL and Stewart Matthews (The University of Queensland). Helpful exchanges with Dr Duncan KEENAN-JONES (UQ School of Historical and Philosophical Inquiry), Ms Sarah MARTIN, Dr Michael WESTAWAY (UQ School of Social Sciences) are acknowledged. The first author thanks Ms Ya-Hui CHOU for her assistance with the drawing. The financial support of the University of Queensland, School of Civil Engineering is acknowledged.

Authors' contributions Hubert Chanson: Conceptualization, Methodology, Formal analysis, Resources, Investigation, Data Curation, Writing—Original Draft, Writing—Review & Editing, Supervision, Visualization, Project administration, Funding acquisition William Johnson: Investigation, Data Curation, Writing—Review & Editing.

Funding The financial support of the University of Queensland, School of Civil Engineering isacknowledged.

Data Availability Some or all data, or models that support the findings of this study are available from the corresponding author upon reasonable request.

Declarations

Conflict of interest The authors have no conflict of interest nor competing interests.

References

1. Bandler H (1995) Water resources exploitation in Australian prehistory environment. Environmentalist 15:97–107
2. Bandler H (2007) Expertise in finding water and exploiting water resources in Australian prehistory. Austr J Water Resouc 11(1):1–11
3. Beal DN, Hover FS, Triantafyllou MS, Liao JC, Lauder GV (2006) Passive propulsion in vortex wakes. J Fluid Mech 549:385–402
4. British Standard (1943). Flow Measurement. *British Standard Code BS 1042:1943*, British Standard Institution, London
5. Chanson H (2014). Applied Hydrodynamics: An Introduction. In: *CRC Press*, Taylor & Francis Group, Leiden, The Netherlands, pp 448 & 21 video movies
6. Chanson H, Brown R (2018) Stability of individuals during Urban inundations: What should we learn from field observations? Geosciences 8(9):341. https://doi.org/10.3390/geosciences8090341
7. Dargin P (1976) Aboriginal fisheries of the Darling-Barwon Rivers. *Brewarrina Historical Society*, Brewarrina NSW, Australia, pp 77
8. Flecker PO (1951) Remains of Aboriginal Habitation on the Great Barrier Wall. The North Queensland Naturalist 19(97):1–3
9. Lapotre MGA, Lamb MP (2015) Hydraulics of floods upstream of horseshoe canyons and waterfalls. J Geophys Res Earth Surf 120:1227–1250. https://doi.org/10.1002/2014JF003412
10. Liao JC, Cotel A (2013) Effects of Turbulence on Fish Swimming. In: Swimming physiology of fish—towards using exercise to farm a fit fish in sustainable aquaculture. *Springer*, (Eds.) Arjan P. Palstra and Joseph V. planas, Chapter 5, pp. 109-127
11. Liggett JA (1994) Fluid mechanics. McGraw-Hill, New York, USA
12. Mathews RH (1903) The aboriginal fisheries at Brewarrina. J Proc Royal Soc New South Wales 37:146–156
13. Pasternack GB, Ellis CR, Leier KA, Valle BL, Marr JD (2006) Convergent hydraulics at horseshoe steps in bedrock rivers. Geomorphology 82:126–145
14. Rowland MJ, Ulm S (2011) Indigenous Fish Traps and Weirs of Queensland. Queensland Archaeol Res 14:1–58
15. Stamataki I, Zang J, Bazeley WD, Morgan GCJ (2014) Study of Flow over weirs such as pulteney weir. In: Proceedings 11th international conference on hydroscience & engineering ICHE 2014, Hamburg, Germany, LEHFELDT & KOPMANN Editors, pp. 295–302

16. Troskolanski AT (1960) Hydrometry: Theory and Practice of Hydraulic Measurements. Pergamon Press, Oxford, UK, p 684
17. Wűthrich D, Pfister M, Schleiss AJ (2020) Forces on buildings with openings and orientation in a steady post-tsunami free-surface flow. Coastal Engineering 161(11):103753
18. Xia J, Falconer RA, Wang Y, Xiao X (2014) New criterion for the stability of a human body in floodwaters. J Hydraulic Res, IAHR 52(1):93–104